Electronic Supplementary Material (ESI) for Journal of Materials Chemistry A.

$Fe_{1-x}S$@S-Doped Carbon Core-Shell Heterostructured Hollow Spheres as Highly Reversible Anode Materials for Sodium Ion Batteries

Qichang Pan,[a] Fenghua Zheng,[a*] Yanzhen Liu,[a] Youpeng Li,[a] Wentao Zhong,[a] Guilin Chen,[a] Junhua Hu,[b] Chenghao Yang,[a*] Meilin Liu[ac]

[a]Guangdong Engineering and Technology Research Center for Surface Chemistry of Energy Materials, New Energy Research Institute, School of Environment and Energy, South China University of Technology, Guangzhou 510006, PR China

[b]School of Materials Science and Engineering, Zhengzhou University, Zhengzhou 450001, China

[c]School of Materials Science & Engineering, Georgia Institute of Technology, Atlanta 30332-0245, Georgia

* Email: Chenghao Yang, esyangc@scut.edu.cn;

Fenghua Zheng, zhengfh870627@163.com

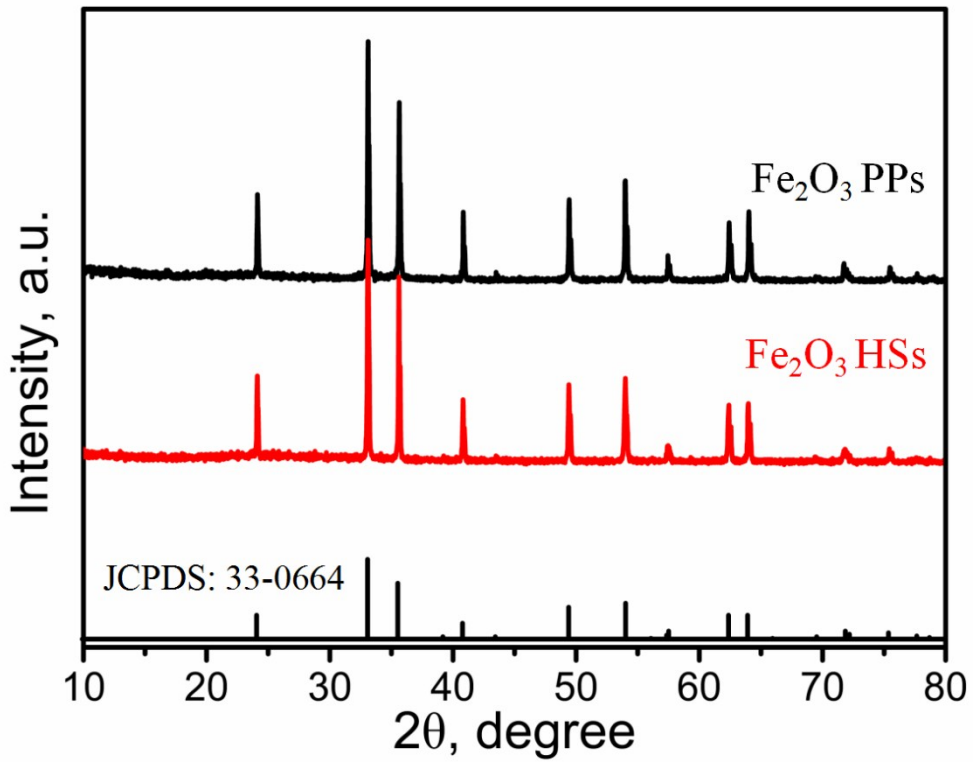

Figure S1 XRD patterns of Fe_2O_3 hollow spheres (Fe_2O_3 HSs) and Fe_2O_3 polyhedral nanoparticles (Fe_2O_3 PPs).

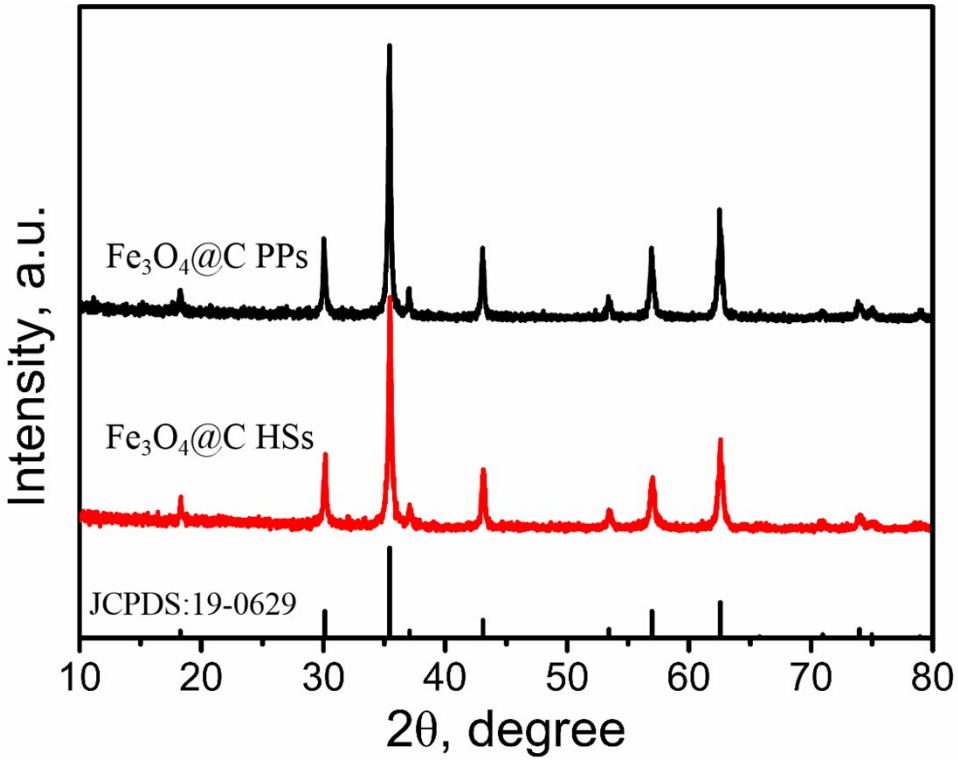

Figure S2 XRD patterns of Fe_3O_4@C HSs and Fe_3O_4@C PPs.

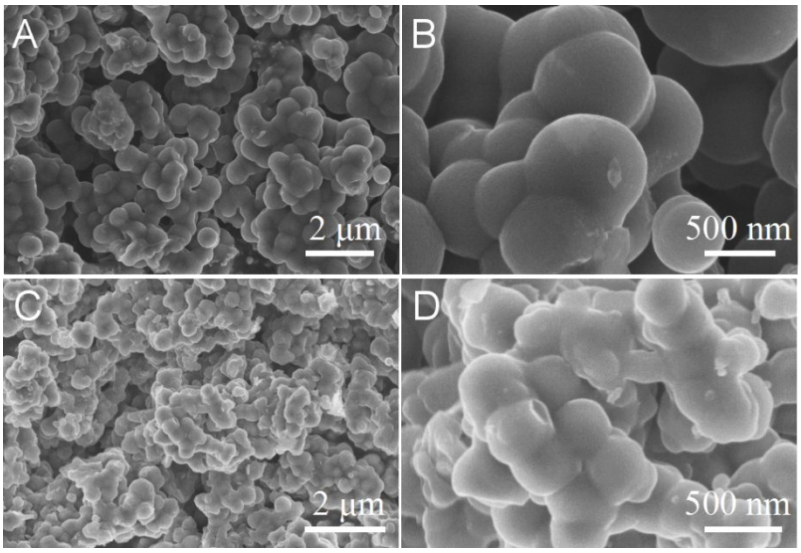

Figure S3 SEM images of (A, B) Fe_3O_4@C HSs and (C, D) Fe_3O_4@C PPs,

respectively.

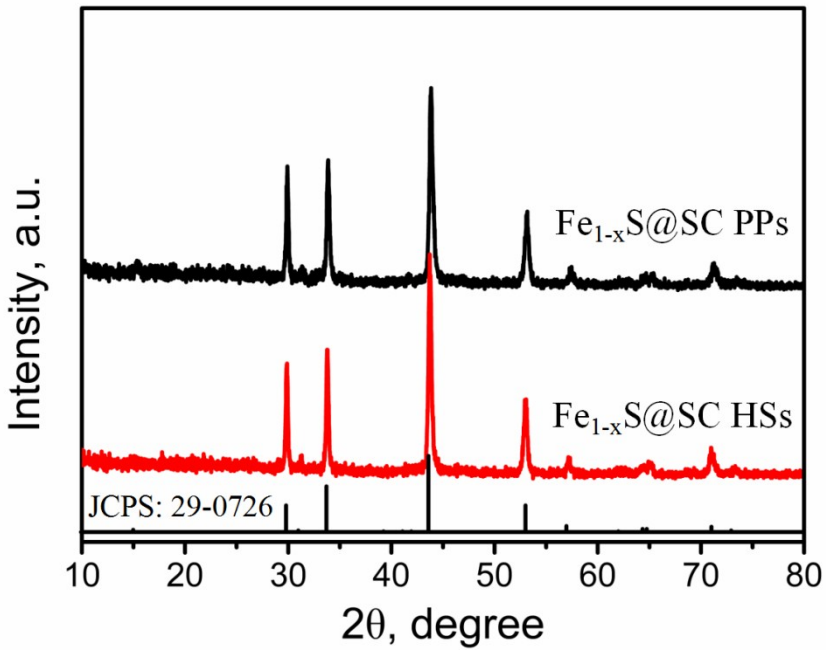

Figure S4 XRD patterns of (A) $Fe_{1-x}S$@SC HSs and (B) $Fe_{1-x}S$@SC PPs.

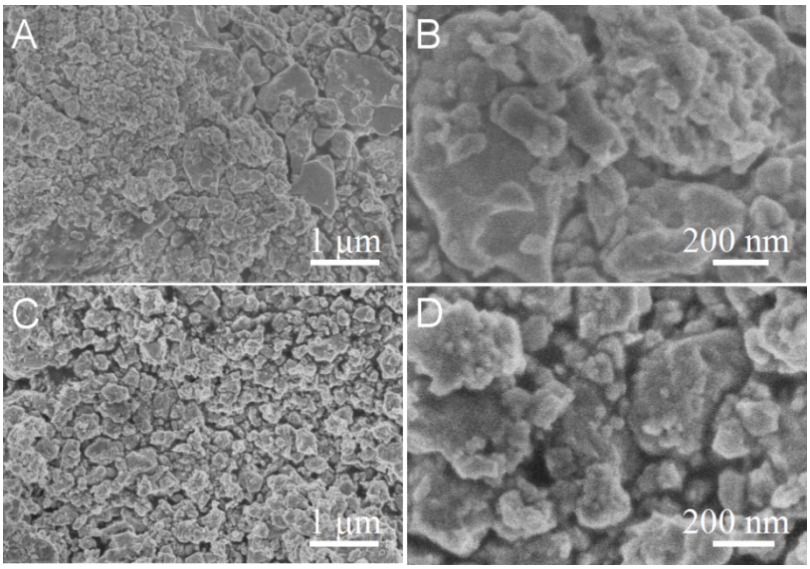

Figure S5 SEM images of pure S-$Fe_{1-x}S$ (A, B), and P-$Fe_{1-x}S$ (C, D) composite, respectively.

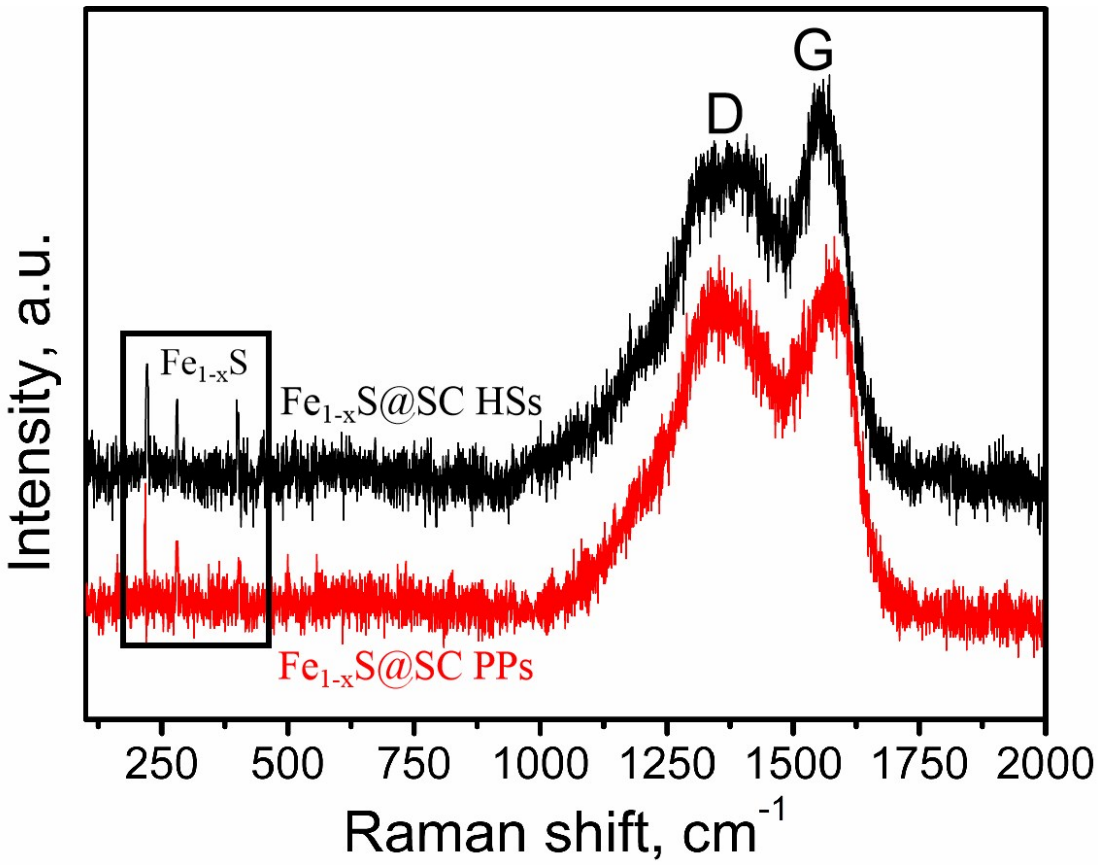

Figure S6 Raman spectra of $Fe_{1-x}S$@SC HSs and $Fe_{1-x}S$@SC PPs.

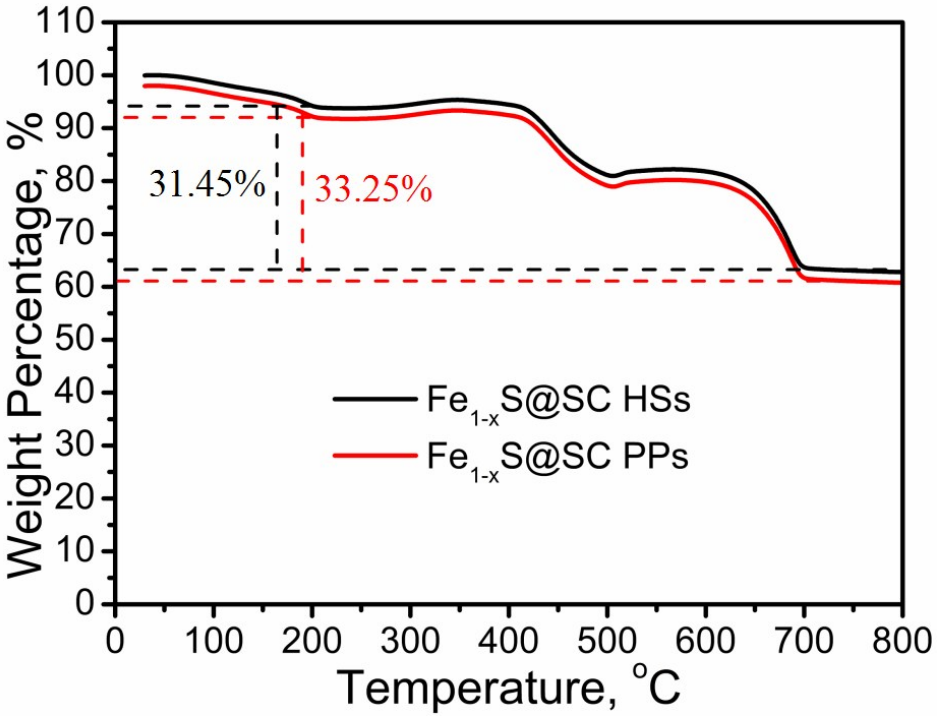

Figure S7 TGA curves of $Fe_{1-x}S$@SC HSs and $Fe_{1-x}S$@SC PPs.

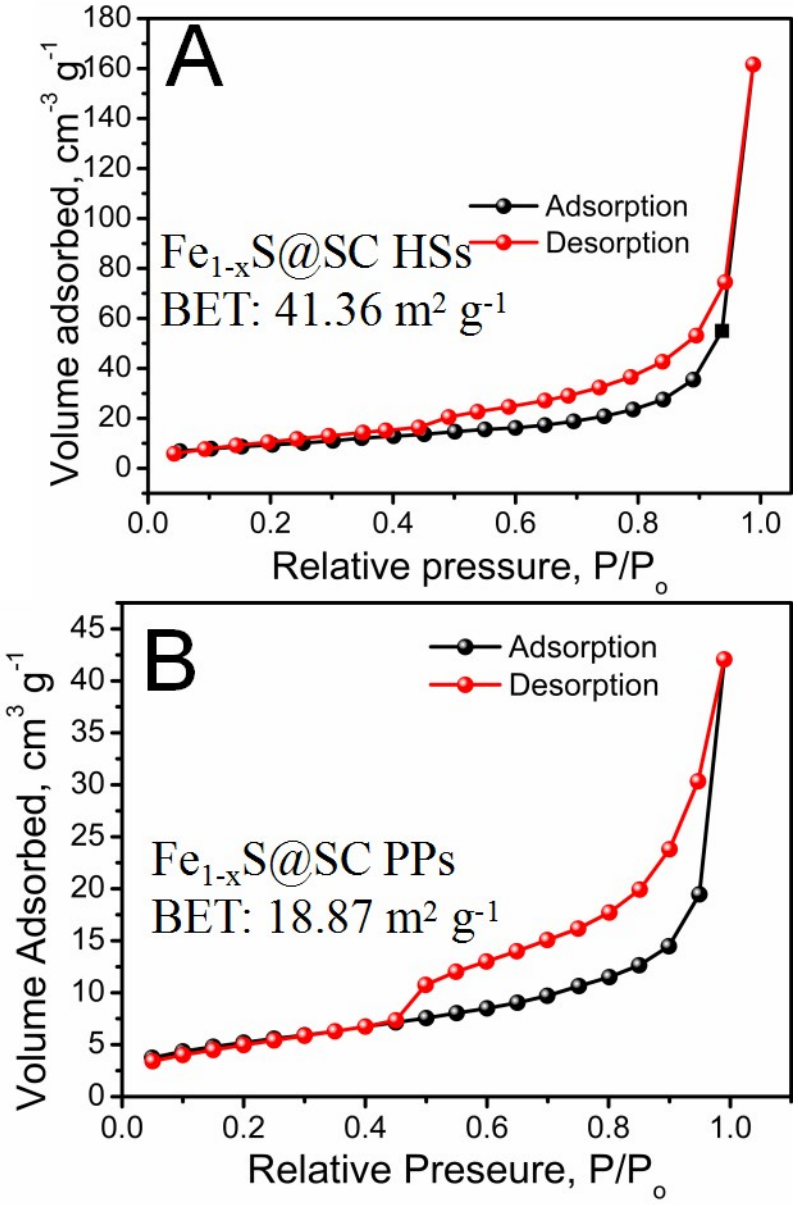

Figure S8 Nitrogen adsorption-desorption isotherm curves of (A) $Fe_{1-x}S$@SC HSs and (B) $Fe_{1-x}S$@SC PPs.

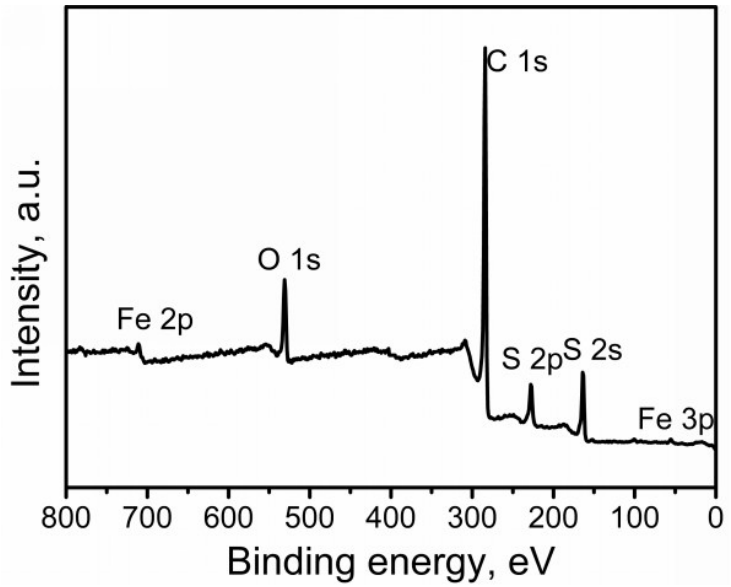

Figure S9 Survey XPS spectra of $Fe_{1-x}S$@SC HSs.

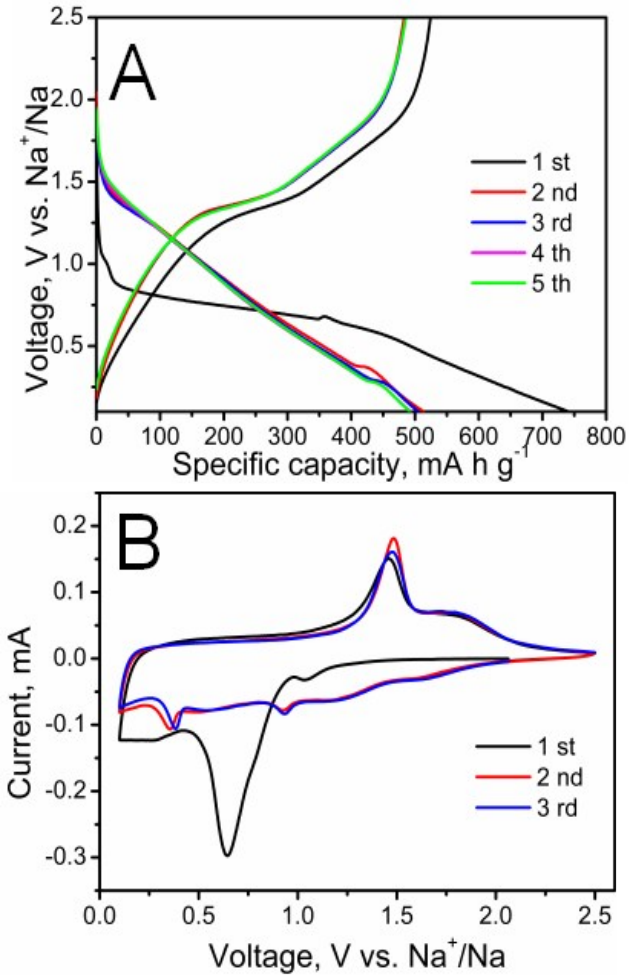

Figure S10 (A) Charge and discharge profiles and (B) CV curves of $Fe_{1-x}S$@SC PPs electrode.

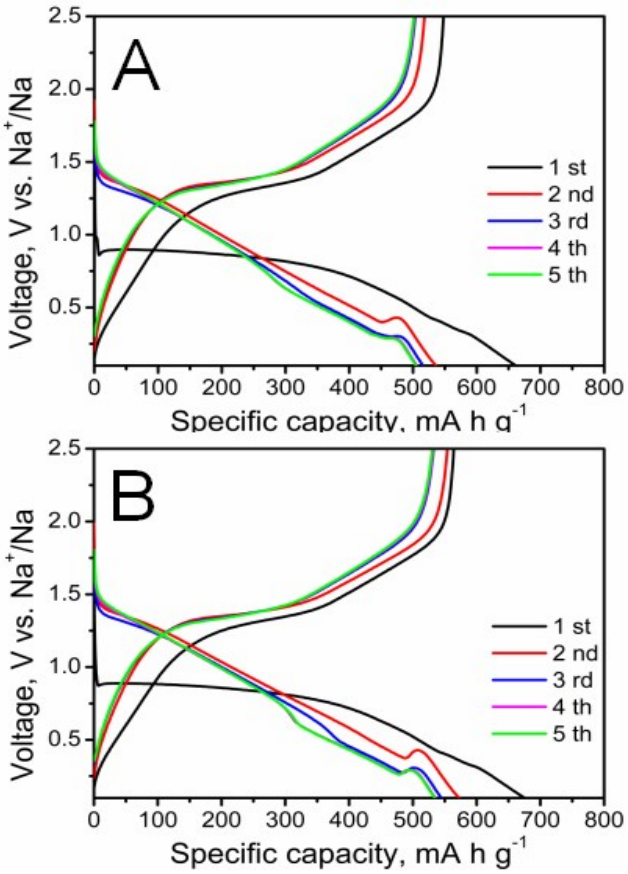

Figure S11 Charge and discharge profiles of pure S-$Fe_{1-x}S$ (A) and P-$Fe_{1-x}S$ (B) electrode.

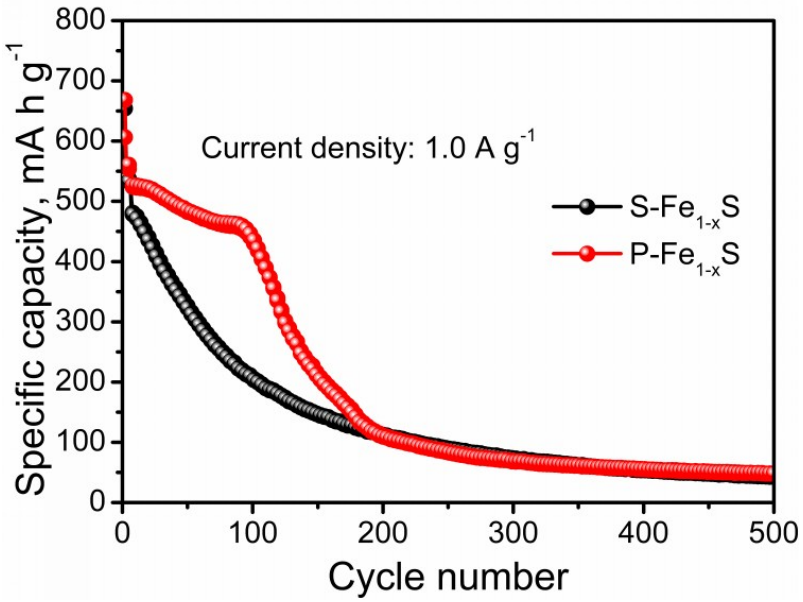

Figure S12 Cycle performance of pure S-$Fe_{1-x}S$, and P-$Fe_{1-x}S$ electrode at 1.0 A g^{-1}.

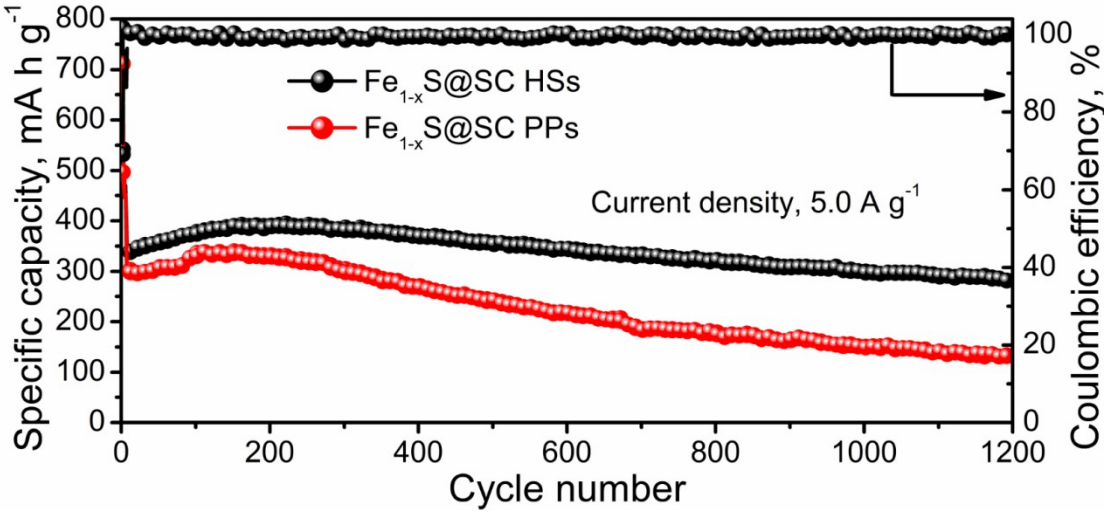

Figure S13 Cycle performance of $Fe_{1-x}S$@SC HSs and $Fe_{1-x}S$@SC PPs at 5.0 A g^{-1}.

Table S1. Comparison of the electrochemical performance of $Fe_{1-x}S$@SC HSs and $F_{1-x}S$@SC PPs with that of reported iron sulfides-based anode materials.

Sample	Capacity, mA h g^{-1}	Cycle number, n	Current density, mA g^{-1}	Reference
FeS@Fe_3C@GC	219.8	200	1.0	15
3DG/FeS@C	358	300	1.0	17
FeS/CA	280	200	0.5	20
$Fe_{1-x}S$@CNTs	449.2	200	0.5	21
porous FeS nanofibers	592	150	0.5	27
$Fe_{1-x}S$@NC@G	385	500	0.2	36
CL-C/FeS	265	200	1.0	37
FeS_x@CS	638.9	100	0.1	38
FeS-rGO	547	50	0.1	S1
FeS@C-N	354.5	500	0.1	S2
FeS/CFs	283	400	1.0	S3
$Fe_{1-x}S$@SC PPs	286	500	1.0	This work
$Fe_{1-x}S$@SC HSs	454.3			

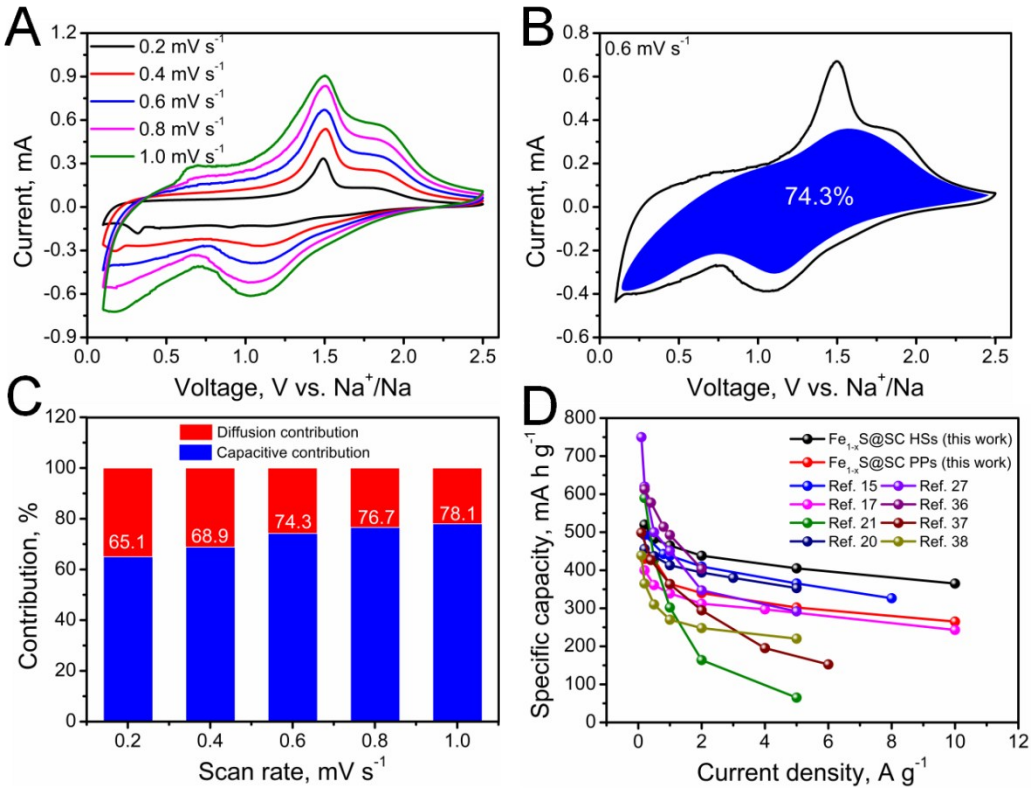

Figure S14 CV curves at various scan rates from 0.2 to 1.0 mV s^{-1} (A), capacitive contribution at 0.8 mV s^{-1} (B), and normalized contribution ratio of capacitive (blue) and diffusion (red) capacities at different scan rates (C) of $Fe_{1-x}S$@SC HSs electrode; comparison of the rate capability of this work with previously reported iron sulfides anodes for SIBs (D).

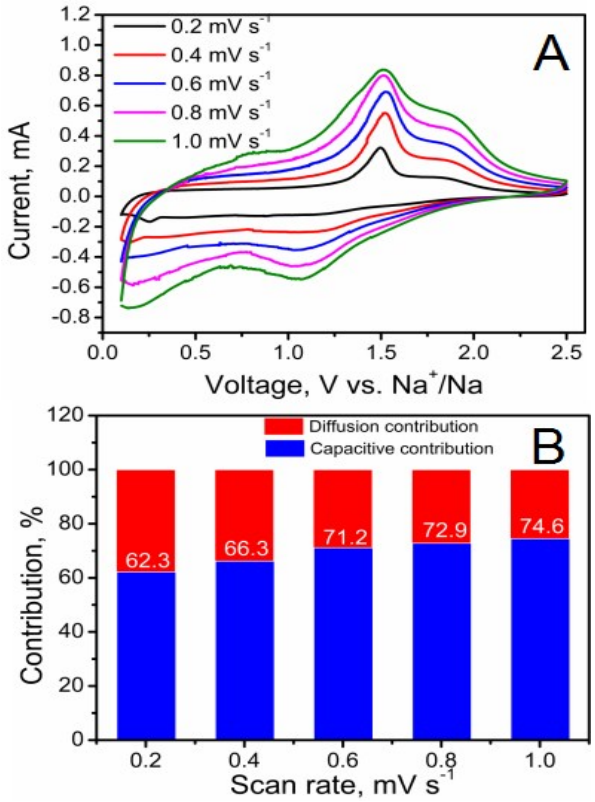

Figure S15 CV curves at various scan rate from 0.2 to 1.0 mV s^{-1} for $Fe_{1-x}S$@SC PPs electrode (A), normalized contribution ratio of capacitive (blue) and diffusion (red) capacities at different scan rates for $Fe_{1-x}S$@SC PPs (B) .

To further understand the high rate capability of the $Fe_{1-x}S$@SC HSs, the capacitive behaviors of the sample was investigated. Figure S15A exhibits the CV curves of $Fe_{1-x}S$@SC HSs electrode at various scan rates range from 0.2 to 1.0 mV s^{-1}. To analyzed the degree of capacitive effect, the following relationship were carried out: $i = av^b$, where i is the peak current corresponding to a particular scan rate (v), a and b are both constants.[S4,S5] Subsequently, the percentage of capacitive and diffusion contributions were determined based on the following equation: $i\ (V) = k_1v^{1/2} + k_2v$. And the equation can be further transformed to the following equation: $i\ (V)/v^{1/2} = k_1+k_2v^{1/2}$. k_1 and k_2 can be facilely achieved by plotting $i(V)/v^{1/2}$ *vs* $v^{1/2}$, and thus the

capacitive current i_c (V) =k_2v could be extracted from the total one with the value of k_2.[S6] As a result, at a given 0.6 mV s^{-1} sweep rate, the CV profile for the capacitive current compared with that of the total measured current is shown in Figure S15B, in which 74.3% is quantified as capacitive. Therefore, the capacitive contributions at 0.2, 0.4, 0.8 and 1.0 mV s^{-1} were also can be measured, and we summarizes the capacitive contributions at various scan rates, the results as shown in Figure S15C. The capacitive contributions are 65.1%, 68.9%, 74.3%, 76.7%, and 78.1% at scan rates of 0.2, 0.4, 0.6, 0.8, and 1.0 mV s^{-1} , respectively. On the other hand, the capacitive contributions at different scan rates for $Fe_{1-x}S$@SC PPs electrode were also investigated based on the same method. Figure S16A shows the CV curves at various scan rates from 0.2 to 1.0 mV s^{-1} for $Fe_{1-x}S$@SC PPs electrode, respectively. And all of the curves at different scan rates exhibit similar shapes, which match well with the $Fe_{1-x}S$@SC HSs electrode. The capacitive contributions at different scan rates for P-$Fe_{1-x}S$@SC electrode were also determined, and the result as shown in Figure S16B. It is worth noting that the $Fe_{1-x}S$@SC HSs electrode exhibits higher capacitive contribution than the $Fe_{1-x}S$@SC PPs electrode, which indicate that the $Fe_{1-x}S$@SC HSs electrode shows more outstanding rate capability compare to $Fe_{1-x}S$@SC PPs electrode, and match well with the rate test results.[S7] Finally, the rate capability of $Fe_{1-x}S$@SC HSs electrode compare to the previously reported iron sulfides anodes for SIBs were summarized (Figure S15D), and suggested that $Fe_{1-x}S$@SC PPs electrode exhibits better rate performance compare to most of previously reported iron sulfides anodes.

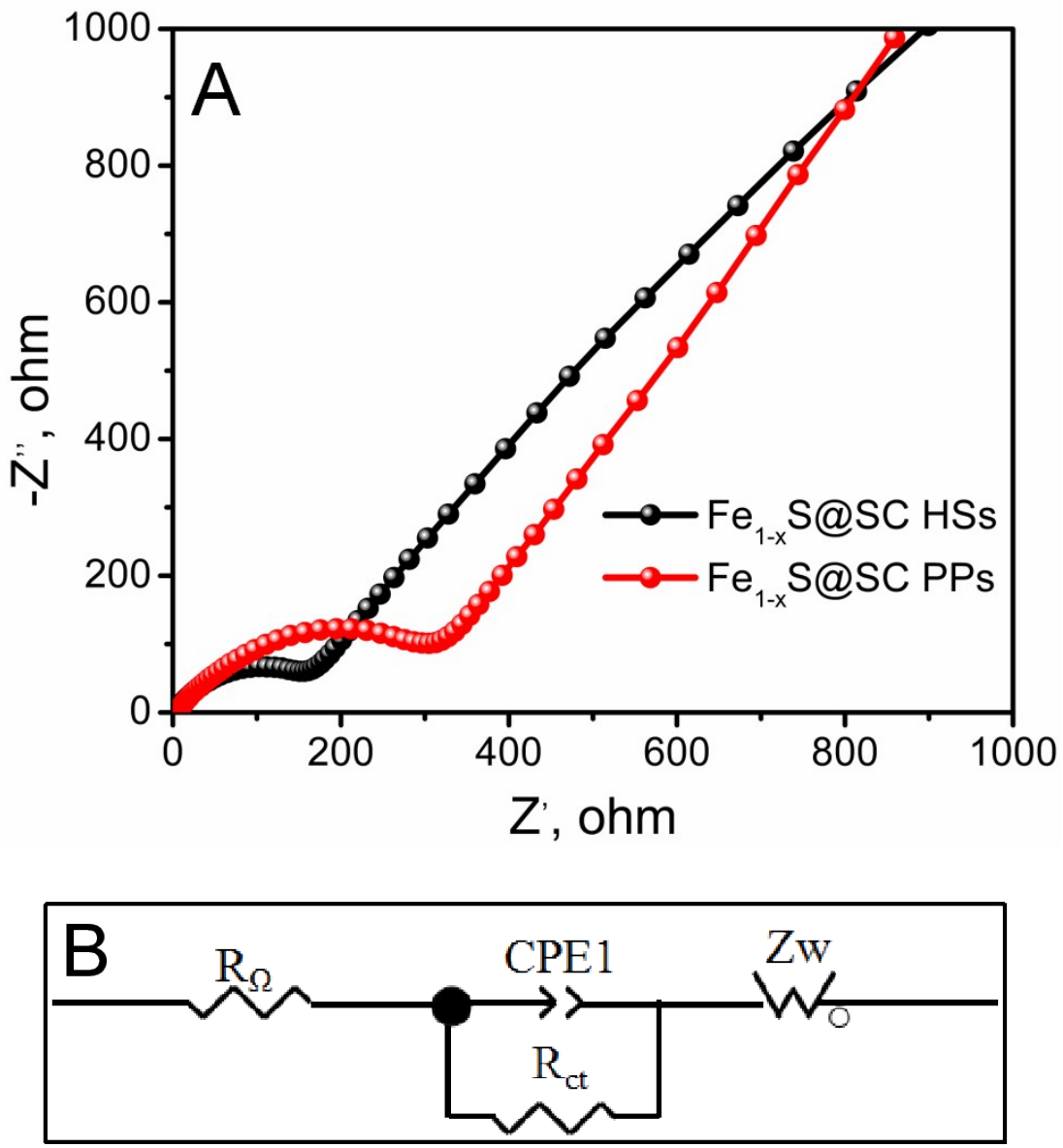

Figure S16 Nyquist plots of as-prepared S-$Fe_{1-x}S$@SC and P-$Fe_{1-x}S$@SC electrode (A), and the equivalent circuit model used for fitting the experimental EIS data (B).

Table S2 Impedance parameters obtained from equivalent circuit model (Figure S16) for $Fe_{1-x}S$@SC HS sand $Fe_{1-x}S$@SC PPs based electrode.

Sample	R_Ω (Ω)	R_{ct} (Ω)	D_{Na}^+ ($cm^2\ s^{-1}$)
$Fe_{1-x}S$@SC HSs	4.8	158.5	6.51×10^{-12}
$Fe_{1-x}S$@SC PPs	7.63	345.3	2.95×10^{-12}

Figure S16 shows the electrochemical impedance spectroscopy (EIS) of $Fe_{1-x}S$@SC HSs and $Fe_{1-x}S$@SC PPs based electrode. The ohmic resistance (R_Ω) and charge transfer resistance (R_{ct}) can be obtained by data fitting according to the equivalent circuit model in Figure S16B, the results are listed in Table S1. The Na^+ diffusion coefficient (D_{Na+}) could be calculated based on Eqs. (S1) and (S2):

$$Z' = R_\Omega + R_{ct} + \sigma\omega^{-0.5} \quad \text{(S1)}$$

$$D_{Na^+} = \frac{(RT)^2}{2(An^2F^2C_{Na^+}\sigma)^2} \quad \text{(S2)}$$

where R, T, A, n, F, C and σ are the gas constant, absolute temperature, contact area of the electrode, number of electrons per molecule during oxidation, Faraday constant, concentration of Na-ions, and Warburg coefficient, respectively.[S8, S9] As a result, the Na^+ ions diffusion coefficient of $Fe_{1-x}S$@SC HSs and $Fe_{1-x}S$@SC PPs are 6.51×10^{-12} and 2.95×10^{-12}, respectively (Table S1). The $Fe_{1-x}S$@SC HSs based electrode exhibits a much higher Na^+ ions diffusion coefficient, and it confirms that the heterostructured hollow spheres can significantly facilitates Na^+ ions diffusion.[S10]

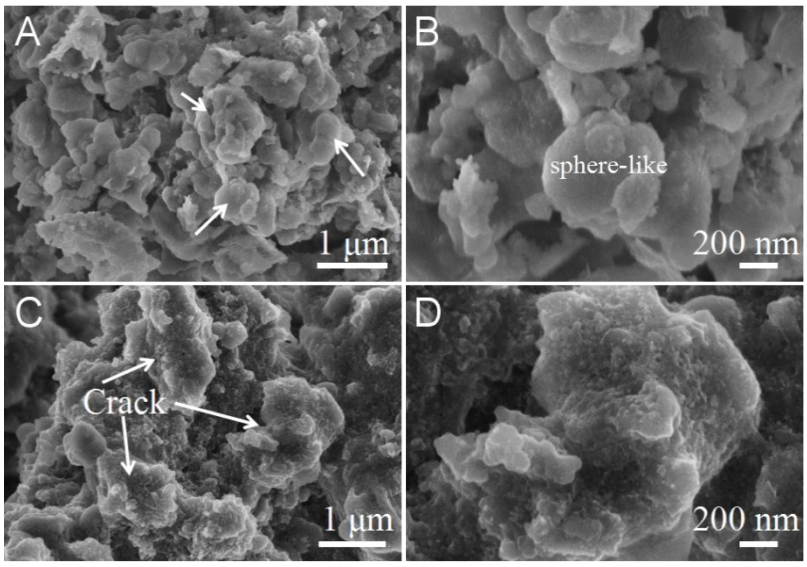

Figure S17 SEM images of $Fe_{1-x}S$@SC HSs (A, B), and $Fe_{1-x}S$@SC PPs (C, D) after 500 cycles at 1.0 A g^{-1}, respectively.

The morphologies of $Fe_{1-x}S$@SC HSs and $Fe_{1-x}S$@SC HSs electrode after long cycles were studied for structural changes. Figure S16 revealed that the SEM images of $Fe_{1-x}S$@SC HSs and $Fe_{1-x}S$@SC PPs electrode after 500 cycles at 1.0 A g^{-1}. Figure S16A and S16B clearly show that the sphere-like structures are almost maintained in the $Fe_{1-x}S$@SC HSs electrode after 500 cycles. But for $Fe_{1-x}S$@SC PPs electrode, polyhedral particles cracked can be obtained after 500 cycles (Figure S16C amd S16D). Therefore, these results further strongly indicated that the S-doped carbon shell and hollow structure can effectively accommodate the large volume change of $Fe_{1-x}S$ and maintain the structural stability during the cycling process.

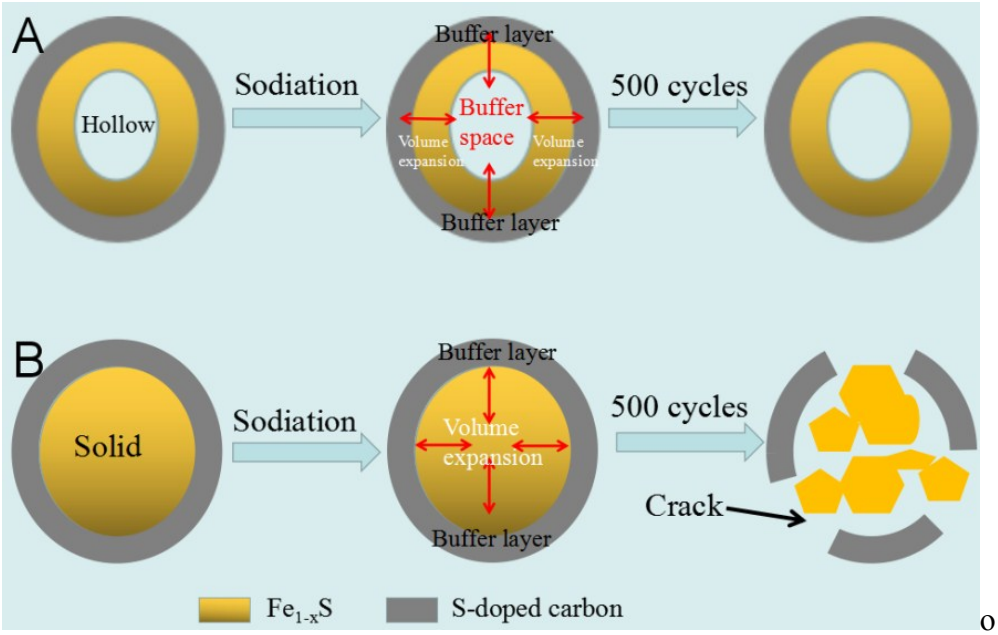

Figure S18 Schematic illustration of $Fe_{1-x}S$@S-doped carbon electrodes during cycling.

References

[S1] S. Y. Lee, Y. C. Kang, Sodium-Ion Storage Properties of FeS-Reduced GrapheneOxide Composite Powder with a Crumpled Structure, Chem. Eur. J., 2016, 22, 2769-2774.

[S2] Z. G. Wu, J. T. Li, Y. J. Zhong, J. Liu, K. Wang, X. D. Guo, L. Huang, B. H. Zhong, S. G. Sun, Synthesis of FeS@C-N hierarchical porous microspheres for the applications in lithium/sodium ion batteries, J. Alloy. Compd., 2016, 688, 790-797.

[S3] D. H. Li, Y. Y. Sun, S. Chen, J. Y. Yao, Y. H. Zhang, Y. Z. Xia, D. J. Yang, Highly Porous FeS/Carbon Fibers Derived from Fe-Carrageenan Biomass: High-capacity and Durable Anodes for Sodium-Ion Batteries, ACS Appl. Mater. Interfaces, 2018, 10, 17175-17182.

[S4] Q. B. Guo, Y. F. Ma, T. T. Chen, Q. Y. Xia, M. Yang, H. Xia, Y. Yu, Cobalt Sulfide Quantum Dot Embedded N/S-Doped Carbon Nanosheets with Superior Reversibility and Rate Capability for Sodium-Ion Batteries, ACS Nano 2017, 11, 12658-12667.

[S5] K. Zhang, M. H. Park, L. M. Zhou, G. H. Lee, W. J. Li, Y. M. Kang, J. Chen, Urchin-Like $CoSe_2$ as a High-Performance Anode Material for Sodium-Ion Batteries, Adv. Funct. Mater. 2016, 26, 6728-6735.

[S6] X. J. Xu, J. Liu, Z. B. Liu, J. D. Shen, R. Z. Hu, J. W. Liu, L. Z. Ouyang, L. Zhang, M. Zhu, Robust Pitaya-Structured Pyrite as High Energy Density Cathode for High-Rate Lithium Batteries. ACS Nano, 2017, 11, 9033-9040.

[S7] X. Xu, R. S. Zhao, W. Ai, B. Chen, H. F. Du, L. S. Wu, H. Zhang, W. Huang, T.

Yu, Controllable Design of MoS_2Nanosheets Anchored on Nitrogen-Doped Graphene: Toward Fast Sodium Storage by Tunable Pseudocapacitance, Adv. Mater. 2018, 30, 1800658.

[S8] F. H. Zheng, Q. Deng, W. T.Zhong, X.Ou, Q. C. Pan, Y. Z. Liu,X. H.Xiong, C. H. Yang, Y. Chen, and M. L. Liu, Fluorine-Doped Carbon Surface Modification of Li-Rich Layered Oxide Composite Cathodes for High Performance Lithium-IonBatteries, ACS Sustainable Chem. Eng. 2018, 6, 16399−16411.

[S9] Y. Z. Liu, W. T. Zhong, C. H. Yang,Q. C. Pan, Y. P. Li, G. Wang, F. H. Zheng,X. H.Xiong, M. L. Liu and Q. Y. Zhang, Direct synthesis of FeS/N-doped carbon composite for high-performance sodium-ion batteries, J. Mater. Chem. A, 2018, 6, 24702-24708.

[S10] Q. C. Pan, Y. G. Huang, H. Q. Wang, G. H. Yang, L. C. Wang, J. Chen, Y. H. Zan, Q. Y. Li, MoS_2/C nanosheets Encapsulated Sn@SnO_x nanoparticles as high-performance Lithium-iom battery anode material, Electrochim.Acta 197 (2016) 50-57.